Influence of Irradiation on Defect Spin Coherence in Silicon Carbide

C. Kasper,[1] D. Klenkert,[1] Z. Shang,[2] D. Simin,[1] A. Gottscholl,[1] A. Sperlich,[1] H. Kraus,[3] C. Schneider,[4] S. Zhou,[2] M. Trupke,[5] W. Kada,[6] T. Ohshima,[7] V. Dyakonov,[1] and G. V. Astakhov[2,1,*]

[1] *Experimental Physics 6 and Würzburg-Dresden Cluster of Excellence ct.qmat, Julius-Maximilian University of Würzburg, 97074 Würzburg, Germany*

[2] *Helmholtz-Zentrum Dresden-Rossendorf, Institute of Ion Beam Physics and Materials Research, 01328 Dresden, Germany*

[3] *Jet Propulsion Laboratory, California Institute of Technology, Pasadena, California 91109, USA*

[4] *Helmholtz-Zentrum Dresden-Rossendorf, Institute of Radiation Physics, 01328 Dresden, Germany*

[5] *Vienna Center for Quantum Science and Technology, Universität Wien, 1090 Vienna, Austria*

[6] *Faculty of Science and Technology, Gunma University, Kiryu, Gunma 376-8515, Japan*

[7] *National Institutes for Quantum and Radiological Science and Technology, Takasaki, Gunma 370-1292, Japan*

(Received 16 August 2019; accepted 18 March 2020; published 21 April 2020)

Irradiation-induced lattice defects in silicon carbide (SiC) have already exceeded their previous reputation as purely performance inhibiting. With their remarkable quantum properties, such as long room-temperature spin coherence and the possibility of downscaling to single-photon-source level, they have proven to be promising candidates for a multitude of quantum-information applications. One of the most crucial parameters of any quantum system is how long its quantum coherence can be preserved. By using the pulsed optically detected magnetic resonance (ODMR) technique, we investigate the spin-lattice relaxation time (T_1) and spin-coherence time (T_2) of silicon vacancies in 4*H*-SiC created by neutron, electron, and proton irradiation in a broad range of fluences. We also examine the effect of irradiation energy and sample annealing. We establish a robustness of the T_1 time against all types of irradiation and reveal a universal scaling of the T_2 time with the emitter density. Our results can be used to optimize the coherence properties of silicon-vacancy qubits in SiC for specific tasks.

DOI: 10.1103/PhysRevApplied.13.044054

I. INTRODUCTION

Defect spins in silicon carbide (SiC) attract growing interest because of their high potential as multidimensional qubits—the so-called qudits—for wafer-scale quantum-information processing at room temperature [1–4]. Particularly, silicon vacancies (V_{Si}) and divacancies (VV) demonstrate an extremely long spin-lattice relaxation time (T_1) and spin-coherence time (T_2), even in commercial wafers without isotope purification [5–12]. These defects can be used for room-temperature quantum metrology [13–16], including magnetometry [17–22] and thermometry [17,23]. Furthermore, single defects have been isolated, which can be used as single-photon emitters [24,25], and coherent control of single-defect spins [26,27] with high fidelity [28–30] has been realized.

SiC itself is a technologically highly developed wide band-gap semiconductor with unique mechanical, electrical, and optical properties, which make it very attractive for various electronic and optoelectronic applications under extreme conditions. Therefore, it is a unique platform to implement hybrid quantum systems, where defect spins can be coupled to the eigenmodes of mechanical resonators [31,32] and photonic cavities [33–36] or integrated into photoelectronic circuits [37–39]. Because SiC is a biocompatible material, the fabrication of spin-carrying defects in SiC nanocrystals [40,41] gives an opportunity for *in vivo* imaging of chemical processes.

Various approaches can be used to create intrinsic defects in SiC, including thermal quenching [1] and laser writing [42]. However, the most common and frequently used methods are based on electron [43,44], neutron [25,45], and ion [46–51] irradiation. There is no optimum irradiation method, as they all have their own advantages and disadvantages, which are schematically presented in Fig. 1.

The irradiation with neutrons generates a homogeneous distribution of silicon vacancies in bulk crystals [Fig. 1(a)]. In combination with high irradiation fluences, this method allows the creation of high-density V_{Si} ensembles, as required for the realization of room-temperature masers

*g.astakhov@hzdr.de

 © 2020 American Physical Society

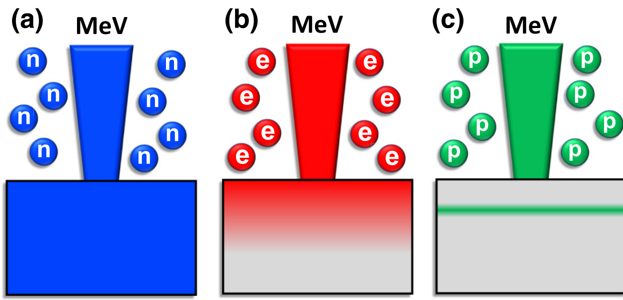

FIG. 1. Schematic generation of the V_{Si} defects in SiC by MeV energy particle irradiation. (a) Neutron irradiation leads to a homogeneous distribution of the V_{Si} defects in the crystal. (b) Electrons show a penetration depth depending on the electron energy. It varies between several 100 μm to several mm for the electron energy between 1 and 25 MeV, respectively. (c) Ion irradiation (e.g., protons) results in the formation of a V_{Si} layer at a depth depending on the ion energy. For instance, the Bragg peak of protons with an energy of 1.7 MeV in SiC is located at a depth of 26 μm below the irradiated sample surface.

[13] and highly sensitive magnetic field sensors [20]. Since neutrons are not charged, they lose almost all of their energy in collisions with nuclei in the lattice and hence considerably damage the SiC crystal. This leads to the creation of a multitude of defect types other than V_{Si} up to the formation of defect clusters, resulting in a deterioration of the V_{Si} coherence properties.

A more gentle approach is electron irradiation [Fig. 1(b)] as a large part of their energy is lost in interactions with crystal electrons. However, the electron damage cannot (in reasonable beam time with common accelerators) reach the quantum center densities achievable after irradiation with neutrons in nuclear reactors. Furthermore, the electron irradiation leads to a quantum center density gradient in the sample, with highest density close to the surface. The electron penetration depth depends on its kinetic energy. For thin samples (up to 100 μm) and MeV-electron energy, the inhomogeneity of the in-depth defect distribution is marginal and can be neglected [52]. However for thick (> 1 mm) samples, the in-depth inhomogeneous distribution should be taken into account. The samples in this study have a thickness of about 300 μm.

In contrast to the aforementioned methods, ions show an increasing stopping power for lower energies according to the Bethe-Bloch equation [53]. This results in the formation of a defect layer at a depth corresponding to the so-called Bragg peak [Fig. 1(c)]. This approach can be used to write 3D defect structures in a SiC crystal using a focussed ion beam [47], allowing the creation of defect spins in the desired place of a nanostructure. On the other hand, the ion irradiation is not suitable for the creation of defect spin ensembles with an in-depth homogeneous distribution.

Any type of irradiation results in the creation of various types of defects, which also change the coherence properties of the vacancy-related spins. The impact of the irradiation on the T_1 and T_2 times, in spite of their crucial importance for quantum applications, has not been systematically investigated so far. In this work, we compare the V_{Si} spin relaxation and spin coherence in SiC created by neutron, electron, and proton irradiation. Particularly, T_1 and T_2 times are measured in a broad range of the density of optically active quantum centers in the infrared regime (from here on referred to as emitter density N_V), from dense ensembles down to isolated defects. To improve the coherence of the V_{Si} defects after irradiation, we also examine the influence of sample annealing. Our results allow the prediction of the V_{Si} spin-coherence properties depending on the irradiation type applied, fluence and particle energy as well as the optimization of the irradiation parameters for a variety of quantum applications. Furthermore, because the initial material is crucial for the performance of SiC quantum devices, our findings can be used as a sensitive probe of the purity of SiC materials. In our experiments, we use commercial high-purity semi-insulating (HPSI) 4*H*-SiC wafers from the leading companies on the SiC market. Because of their relatively low-fabrication cost and mass-scale production, these wafers are considered for the practical realization of room-temperature SiC-based quantum devices.

II. METHODS

Neutron irradiation is performed in two different research reactors. For the first irradiation set, we purchase a high-purity semi-insulating (HPSI) 3-inch SiC wafer from CREE and use chambers DBVK and DBVR at the BER II reactor at Helmholtz-Zentrum Berlin. Since thermal neutrons produce negligible displacement, only epithermal and fast neutrons are counted in the fluence calculation [54]. The neutron fluence spanned a large range from 3.3×10^{16} cm^{-2} to 3.5×10^{19} cm^{-2}. For the second irradiation set, we purchase a HPSI SiC wafer from Norstel and use the TRIGA Mark II reactor (General Atomics, San Diego) of the Atominstitut, TU Wien [25]. During irradiation, the temperature of the crystals did not exceed 100 °C. Vacancy creation by neutron irradiation in SiC is weakly dependent on neutron energy in the range 0.18 MeV < E_n < 2.5 MeV, but falls off rapidly for smaller energies. The neutron energies in the TRIGA reactor are distributed evenly in the range between 100 eV and 1×10^5 eV, with a peak in flux density around 2.5 MeV followed by a sharp cut-off.

For the electron-irradiated sample series, a HPSI 3-inch 4*H*-SiC wafer is purchased from Norstel and diced into many pieces. The irradiation with electron energies of 1 and 2 MeV is performed at the electron-beam irradiation facility at QST Takasaki (Japan). During the irradiation,

the samples are placed on a water-cooled copper plate to avoid heating by the electron beams. The irradiation with electron energies of 20 and 25 MeV is performed at the electron accelerator ELBE in HZDR (Germany). The beam is extracted through a 300 μm beryllium vacuum window and passes 150 mm through air before hitting the sample. The incident beam distribution and the small angle scattering in the vacuum window and air leads to a Gaussian-shaped beam distribution on the sample. The beam profile is measured at the position of the sample with a Roos ionization chamber (IC) N34001. The certificate calibrated IC and a Faraday cup are used for the dose and current calibration. From the profile measurement, the irradiation parameters are deduced. To monitor the current stability of the electron gun as well as dark-current contributions, the edge field of the beam is constantly measured and stabilized during the irradiation.

Proton irradiation is done at the TIARA irradiation facilities in Takasaki, Japan. A piece of a 4H-SiC wafer purchased from CREE is placed on an aluminum plate and irradiated with a focused proton beam generated by a single-ended particle accelerator with a typical spot size of 1 μm $\times$ 1 μm and proton energy of 1.7 MeV. The irradiation beam current is monitored by a beam dump (Faraday cup) connected to a picoampermeter before and after irradiation.

The continuous wave and pulsed ODMR measurements are performed with a confocal setup. For optical excitation, a 788-nm diode laser (LD785-SE400 from Thorlabs) is coupled into a 50 μm optical fiber and focused onto the sample using a $\times 10$ objective (Olympus LMPLN10XIR), with the laser spot measuring approximately 10 μm in diameter. The laser power at the surface of the sample is about 20 mW. The collection volume is approximately 300 μm^3 in case of electron- and neutron-irradiated samples. For the measurement of the proton-irradiated sample, a $\times 100$ objective (Olympus LCPLN100XIR) is used, which leads to a collection volume of approximately 2.6 μm^3. The PL is collected through the same objective and separated from the scattered laser light using a 850 nm short-pass dichroic mirror and a 875-nm-long pass filter. Behind the filter, it is coupled into a 600 μm optical fiber and detected using a Si avalanche photodiode (APD120A from Thorlabs). The sample is placed on a 0.5-mm copper stripline to apply the microwaves generated by a signal generator (Stanford Research Systems SG384) and amplifier (Vectawave VBA1000-18). A permanent magnet is mounted below the sample to generate the external magnetic field of 15 mT. To generate the laser pulses needed for time-resolved ODMR experiments, an acousto-optic modulator (Opto-Electronic MT250-A02-800) is placed in the laser beam path. The microwaves are modulated using an rf switch (Mini-Circuits ZASWA-2-50DR+). TTL pulsing for laser and microwave modulation is provided by a PulseBlaster ESR-PRO 500 MHz card from SpinCore. The ODMR signal is processed using either a lock-in amplifier (Signal Recovery DSP 7230) or an oscilloscope card from GaGe CompuScope (Razor Max).

III. RESULTS

Figure 2(a) shows the modification of the optical properties of a SiC crystal with increasing neutron irradiation fluence. The irradiation is performed in nuclear-research reactors. Since thermal neutrons only produce negligible displacement, only epithermal and fast (MeV) neutrons are counted in the fluence calculation [54]. SiC is a wide band-gap semiconductor with a band gap of 3.23 eV and is therefore transparent in the case of the lowest neutron fluence $\Phi_n = 9.2 \times 10^{15}$ cm^{-2}. Neutron irradiation creates a variety of optically active and inactive defects, which has a direct effect on the optical properties of the crystal due to absorption and scattering of light by the

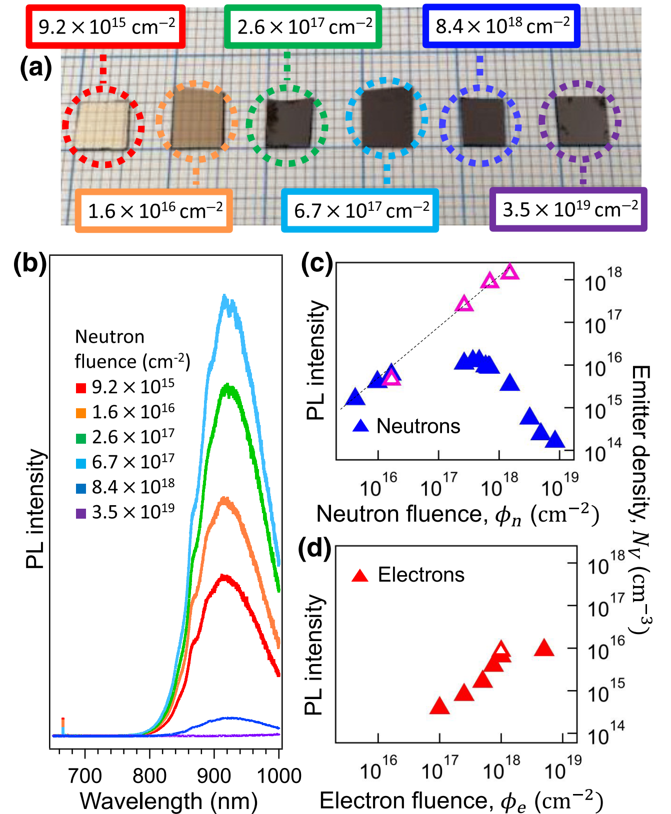

FIG. 2. Irradiation impact on the optical properties of SiC. (a) Photographs of the SiC crystals for different neutron irradiation fluences. (b) PL spectra of the V_{Si} defects for different neutron irradiation fluences. (c) Variation of the PL intensity and corresponding emitter density as a function of the irradiation fluence with epithermal and fast neutrons. (d) Same as (c) for 2-MeV electrons. Open triangles in (c) and (d) show the V_{Si}(V2) density obtained from the quantitative EPR experiments. The dashed line in (c) is a fit to $N_V = C(\Phi_n)^\alpha$ with $\alpha = 0.8$ [25].

defects. High irradiation fluences cause crystal destruction and in the case of the highest neutron fluence $\Phi_n = 3.5 \times 10^{19}$ cm^{-2}, SiC becomes completely opaque. The generation of the V_{Si} defects is verified by their characteristic room-temperature PL band in the near-infrared (NIR) spectral range of 800–1000 nm [55], as shown in Fig. 2(b). The V_{Si} PL intensity shows nonmonotonic behavior with the irradiation fluence. This is because high irradiation fluences lead to crystal damage and the creation of other types of defects (including defect clusters) providing nonluminescent relaxation paths for the V_{Si} defects.

To find the emitter density N_V, we calibrate the PL intensity in our confocal setup with a defined collection volume using a 4H-SiC sample with known N_V [25]. Figure 2(c) presents the concentration of the optically active V_{Si} defects as a function of the neutron fluence, which is varied over more than 3 orders of magnitude. The maximum $N_V = 2 \times 10^{16}$ cm^{-3} is observed for $\Phi_n = 6.7 \times 10^{17}$ cm^{-2} and dramatically drops down for the higher neutron fluences. The electron-irradiated samples reveal qualitatively similar behavior. Figure 2(d) presents N_V as a function of the electron fluence Φ_e for an electron energy of $E_e = 2$ MeV. The maximum $N_V = 1 \times 10^{16}$ cm^{-3} is achieved for $\Phi_e = 4 \times 10^{18}$ cm^{-2}. A higher Φ_e than Φ_n is required to achieve the respective maximum N_V in our samples, pointing at a lower V_{Si} creation yield in the case of electron irradiation compared to neutron irradiation.

The crystallographic V_{Si} configuration is schematically presented in Fig. 3(a). The capture of an electron by a silicon vacancy, in addition to the four electrons from the surrounding carbon atoms leads to a negatively charged state. Only this charge configuration of V_{Si} is optically active in NIR. Two of the total five electrons build a spin singlet and the three remaining electrons form a spin quadruplet with $S = 3/2$ [13]. Upon laser excitation at 785 nm, the radiative recombination from the excited-state (ES) to the ground-state (GS) leads to the characteristic NIR PL of the V_{Si} defects, as presented in the energetic structure of Fig. 3(b). There are two types of the V_{Si} defect in the 4H-SiC polytype, referred to as $V1$ and $V2$ centers [43].

In this study, we concentrate on the $V2$ center with the characteristic zero-phonon line (ZFL) at 917 nm and the zero-field splitting (ZFS) of 70 MHz between the GS spin sublevels $m_S = \pm 1/2$ and $m_S = \pm 3/2$. There is also spin-dependent recombination from the ES to the GS through a metastable-state (MS), resulting in the preferential population of the $m_S = \pm 1/2$ spin sublevel [Fig. 3(b)]. The PL intensity is higher for the $m_S = \pm 3/2$ spin state, which is the basis for the optically detected magnetic resonance (ODMR) experiments with microwave- (MW) induced transitions between the GS spin sublevels [17]. In the absence of an external magnetic field ($B = 0$ mT), the ZFS can directly be observed in the ODMR spectrum [Fig. 3(c)]. The ODMR contrast is calculated as the MW-induced PL change (ΔPL) divided by the PL intensity, i.e., ΔPL/PL. In an external magnetic field ($B \neq 0$ mT), the GS spin sublevels are split as shown in the inset of Fig. 3(c). This results in two ODMR lines at the MW frequencies $\nu_{1,2} = |\mathrm{ZFS} \pm \gamma B|$, where $\gamma = 28$ MHz/mT is the electron gyromagnetic ratio. An example of an ODMR spectrum at $B = 15$ mT is shown in Fig. 3(c).

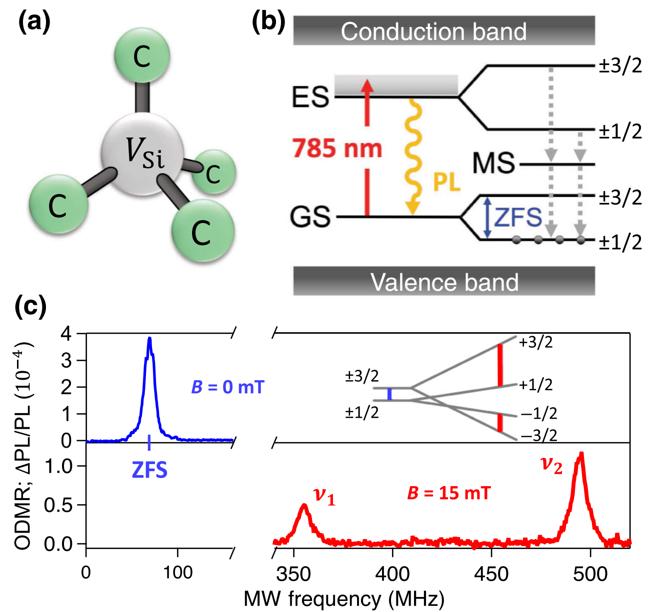

FIG. 3. (a) Schematic presentation of a single V_{Si} defect. (b) Energy and spin structure of the negatively charged V_{Si} defect with $S = 3/2$. The solid arrow represents laser excitation, the wave arrow represents the radiative recombination and the dashed arrows represent the spin-dependent relaxation. (c) Room-temperature ODMR spectra of a V_{Si} ensemble without applied magnetic field (blue) and in an external magnetic field $B = 15$ mT (red). The inset shows the Zeeman splitting of the spin sublevels with corresponding transitions represented by the vertical lines.

We employ quantitative electron paramagnetic resonance (EPR) to alternatively measure the defect density. The EPR signal intensity is proportional to the absolute number of spins and hence, by comparing to a known reference sample, the absolute spin number can be obtained. We use the typical EPR reference 1,3-bis(diphenylene)-2-phenylallyl (BDPA)—a molecular radical with one spin per molecule. The molecular weight is known and the sample weight is carefully measured to yield an absolute spin standard. The reference and SiC samples are measured in the same spectrometer with the same settings in the dark (i.e., without laser excitation) at room temperature to ensure comparability (Fig. 4). A typical EPR spectrum of the the V2 spin $S = 3/2$ defect in SiC consists of three transitions [13]. The center transition at $g = 2$ accompanied by the lower and higher magnetic field transitions. We use the lower-field transition as at this magnetic

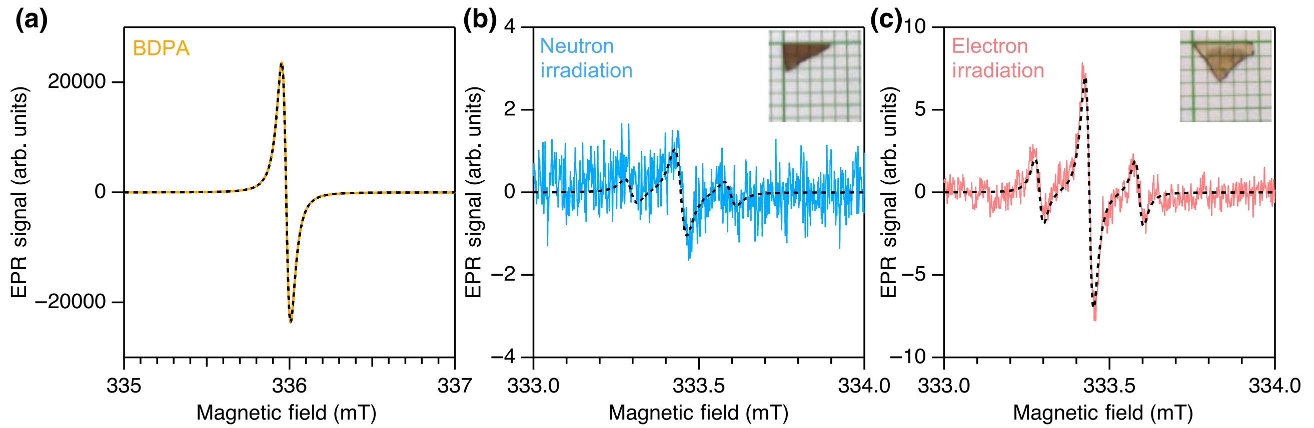

FIG. 4. Determination of the defect density $N_V^{\rm EPR}$ from quantitative EPR spectra at room temperature. (a) Reference sample of molecular BDPA radicals with known spin number $n_{\rm BDPA} = 3.6 \times 10^{17}$. (b),(c) Low-field EPR transition of the $V2$ defect for the $4H$-SiC samples. The ratio of the double integrated spectral fits (dashed lines) yields absolute $V2$ defect numbers. (b) Irradiation with a neutron fluence $\Phi_n = 1.6 \times 10^{16}$ cm^{-2}. The obtained density is $N_V^{\rm EPR} = 4.5 \times 10^{15}$ cm^{-3}. (c) Irradiation with an electron fluence $\Phi_e = 1 \times 10^{18}$ cm^{-2} yields $N_V^{\rm EPR} = 8.6 \times 10^{15}$ cm^{-3}. The dashed lines are fits as described in the text.

field range, no other EPR transitions are present, resulting in undistorted, background-free spectra. EPR spectra are recorded as the first derivative of the MW absorption spectrum. The integral of the absorption is proportional to the spin number. The relative intensities of the fitted, doubly integrated EPR spectra thus yield absolute spin numbers. In the case of SiC, we fit the main peak of the lower-field transition and its two satellites caused by the hyperfine interaction with ^{29}Si isotopes [1]. Considering the spin of the reference radical ($S = 1/2$) and the $V_{\rm Si}$ defect ($S = 3/2$), as well as the sample geometry, the spin density of the $V2$ centers can be determined. Though this procedure does not take into account the spin density of the $V1$ centers, their concentration is assumed to be comparable to that of $V2$. This leads to some underestimation of the total $V_{\rm Si}$ density.

The $V_{\rm Si}$ density obtained from the quantitative EPR is shown by the open triangles in Figs. 2(c) and 2(d). In the case of neutron irradiation [Fig. 2(c)], the estimation of the $V_{\rm Si}$ density from the PL (N_V) and quantitative EPR ($N_V^{\rm EPR}$) methods gives similar values for $\Phi_n < 1 \times 10^{17}$ cm^{-2}. The nonradiative quenching of the $V_{\rm Si}$ PL is an increasingly dominant process for samples that are subject to high Φ_n, resulting in a depreciation of the defect densities for high fluences. In the case of electron irradiation, we observe a qualitatively good agreement between the PL-based and EPR-based methods for high $\Phi_e = 1 \times 10^{18}$ cm^{-2} [Fig. 2(d)].

To measure the coherence properties of the $V_{\rm Si}$ spins at room temperature, we use pulsed ODMR as schematically presented in Figs. 5(a), 5(c) and 5(e). The pulse sequences are described in detail in earlier works [9,12]. The first laser pulse is used to initialize the system into the $m_S = \pm 1/2$ state. It is followed by a MW pulse to drive the ν_2 spin transition between the $+1/2$ and $+3/2$ spin sublevels [inset of Fig. 3(c)]. We apply a magnetic field $B = 15$ mT along the c axis of the $4H$-SiC crystal to suppress the heteronuclear-spin flip-flop processes and hence the decoherence [6,8]. The second laser pulse is used to reinitialize the system and read out the spin states of the $V_{\rm Si}$ defects. For this purpose, ΔPL/PL, which corresponds to the spin states of the $V_{\rm Si}$ defects, is detected immediately after the laser is switched on [dashed box in Figs. 5(a), 5(b) and 5(d)]. We first measure Rabi oscillations by varying the MW pulse length τ [Fig. 5(a)]. An example of a measurement on an electron-irradiated sample with $\Phi_e = 1 \times 10^{17}$ cm^{-2} corresponding to $N_V = 3.9 \times 10^{14}$ cm^{-3} is presented in Fig. 5(b). The fitting of these data to an exponentially decaying sine wave (solid line) allows the calibration of the MW duration for the π and $\pi/2$ pulses.

To measure the spin-lattice relaxation time T_1 we use the protocol of Fig. 5(c), where the MW π pulse is applied after the variable delay time τ to exchange the spin population between the $m_S = +3/2$ and $m_S = +1/2$ states. The fitting of the experimental data to a monoexponential decay of $\exp(-2\tau/T_1)$ gives the spin relaxation time T_1 [27]. A fitting example is shown in Fig. 5(d) by the solid line. We note that the spin relaxation time between the $m_S = +1/2$ and $m_S = -1/2$ states is expected to be shorter $T_1' = 3T_1/4$ [12].

To measure the spin-coherence time T_2, we use the spin-echo sequence presented in Fig. 5(e). The first $\pi/2$ pulse creates a coherent superposition of the $m_S = +3/2$ and $m_S = +1/2$ states. It is followed by a π pulse to refocus the spin coherence after dephasing and the last $\pi/2$ pulse to project the created superposition to an optically readable state. An example of the experimental data is presented in Fig. 5(f). In addition to an exponential decay, the signal is

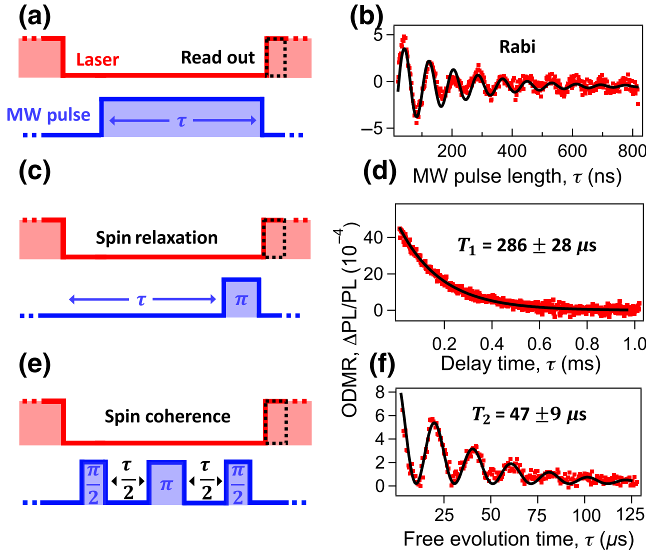

FIG. 5. Coherent control of the V_{Si} defects. (a),(c),(e) Laser and MW pulse sequences to measure Rabi oscillations, spin-lattice relaxation time T_1 and spin-echo coherence time T_2, respectively. For read out of the spin state we use a second laser pulse and collect the PL (dashed box), where τ is a variable parameter. (b),(d),(f) Symbols represent experimental data for Rabi oscillations as well as for T_1 and T_2, respectively. Solid lines are fitting curves as discussed in the main text. Data are obtained at room temperature in a magnetic field of 15 mT. The measured 4H-SiC sample is irradiated with electrons to a fluence $\Phi_e = 1 \times 10^{17}$ cm^{-2} corresponding to $N_V = 3.9 \times 10^{14}$ cm^{-3}.

modulated with a few frequency components, known as the electron spin-echo envelope modulation (ESEEM). These modulations have been shown to arise through hyperfine interactions between the V_{Si} defect spins and the surrounding ^{29}Si and ^{13}C nuclei [7,26,27]. In the case of $S = 3/2$, the modulation frequencies and modulation amplitudes reveal a complex magnetic field dependence. To fit the experimental data, we use the product of oscillating functions decaying as $\exp(-\tau/T_2)$. The details of the fitting procedure are described elsewhere [9]. An example of such a fit (solid line), from which we determine T_2 is shown in Fig. 5(f).

IV. DISCUSSION

A. Effect of irradiation

Figure 6 summarizes the measurements of the spin-lattice relaxation time T_1 and the spin-coherence time T_2 as a function of the emitter density (N_V) in electron, neutron, and proton irradiated samples. Because the emitter density depends nonmonotonically on neutron fluence (Fig. 2), we analyze N_V for $\Phi_n < 6.7 \times 10^{17}$ cm^{-2}.

The T_1 time is quite robust against irradiation for all irradiation types up to $N_V = 7 \times 10^{15}$ cm^{-3} and equals $T_1 \sim 300$ μs. Remarkably, the electron energy in the range

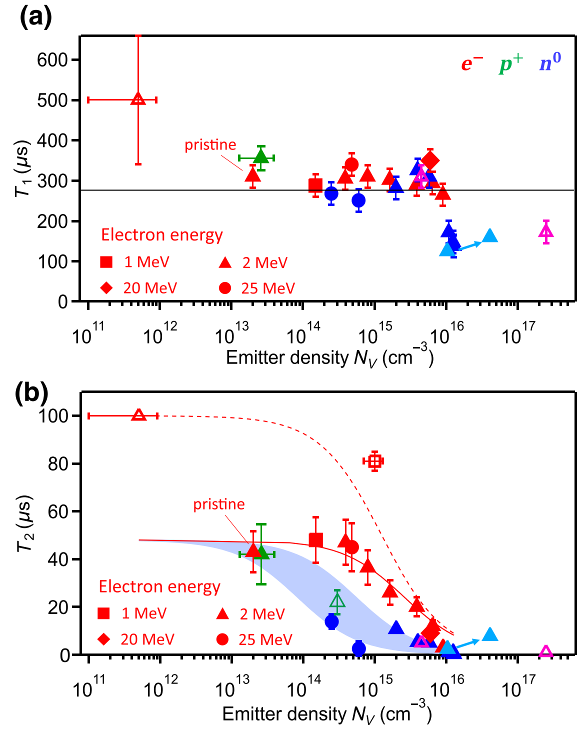

FIG. 6. Spin-coherence properties of the V_{Si} defects in 4H-SiC for different irradiation particles as a function of emitter density. The samples are irradiated with electrons (red), neutrons (blue and cyan), or protons (green). (a) Spin-lattice relaxation time T_1 as a function of the emitter density. The red closed symbols correspond to our measurements with electron energies 1 MeV (squares), 2 MeV (triangles), 25 MeV (circles), and 20 MeV (diamonds). The green triangle corresponds to proton irradiation with an energy of 1.7 MeV [47]. The red open triangle corresponds to a single V_{Si} defect [27]. The T_1 time is a constant around 300 μs for low emitter densities (the solid line) and drops rapidly for high densities due to crystal damage. The blue closed triangles and circles correspond to the neutron irradiation in the BER II reactor in Berlin and in a TRIGA Mark-II reactor in Vienna, respectively. The cyan triangles represent measurements on a neutron-irradiated sample before and after annealing [Fig. 8(a)]. The open magenta triangles represent N_V^{EPR} in neutron-irradiated samples obtained from the EPR experiments [Fig. 2(c)]. (b) Spin-coherence time T_2 as a function of emitter density. The assignment of symbols is the same as in (a). The red (green) open square (triangle) corresponds to an electron (proton) irradiation energy of 2 MeV [7,50]. The red solid and dashed lines as well as the cyan area are fits to Eq. (1) with parameters described in the text.

from 1 to 25 MeV has no effect on T_1. The V_{Si} spin relaxation is dominated by the Raman mechanism of spin-phonon scattering [9,32], which is an intrinsic property of a SiC crystal and hence independent of the irradiation fluence. This result corresponds well to $T_1 = 500 \pm 160$ μs reported for a single V_{Si} defect in a sample with $N_V \sim 10^{11} - 10^{12}$ cm^{-3} [27]. In the case of higher emitter density, the spin relaxation is given by the interaction with

surrounding defects and the T_1 time decreases rapidly with N_V.

The spin coherence time T_2 reveals strong dependence on the irradiation fluence as shown in Fig. 6(b). The spin decoherence is governed by interactions with the surrounding spin bath of nuclei (^{29}Si, ^{13}C) $1/T_2^{(n)}$, paramagnetic centers (particularly ^{14}N) $1/T_2^{(p)}$ as well as residual (particularly carbon vacancies) $1/T_2^{(r)}$, and irradiation-induced defects $1/T_2^{(i)}$ [6,7,56]. The resulting spin decoherence rate is then $1/T_2 = 1/T_2^{(n)} + 1/T_2^{(p)} + 1/T_2^{(r)} + 1/T_2^{(i)}$. By applying a moderate magnetic field $1/T_2^{(n)}$ is suppressed [6]. We assume that $1/T_2^{(i)}$ is proportional to the number of all irradiation-induced defects, which in turn scales with N_V. Under this assumption, the effect of irradiation can be described by

$$T_2 = \frac{T_2^{(\text{pristine})}}{1 + T_2^{(\text{pristine})}\kappa N_V}. \tag{1}$$

Here, $T_2^{(\text{pristine})}$ is the spin-coherence time in a pristine, nonirradiated sample given by the presence of residual paramagnetic centers and nuclear spins. It is therefore depending on the intrinsic properties and quality of a wafer. We assume linear dependence of the spin-dephasing rate on the concentration of paramagnetic centers [57] and obtain $1/T_2^{(i)} = \kappa N_V$ where κ is the coefficient of proportionality.

We now discuss the experimental data for T_2 in the electron-irradiated samples presented in Fig. 6(b). As in the case of the T_1 time, we do not find any significant dependence on the electron energy. In our HPSI wafers (solid symbols) with low irradiation fluence ($\Phi_e < 3 \times 10^{17}$ cm^{-2}, $N_V = 7 \times 10^{14}$ cm^{-3}), the T_2 time is nearly independent of N_V. The experimental data can be well fitted to Eq. (1) with $T_2^{(\text{pristine})} = 48$ μs and $\kappa = 0.8 \times 10^{-11}$ s^{-1} cm^3 [solid line in Fig. 6(b)]. A deviation towards lower values is observed for $N_V > 7 \times 10^{15}$ cm^{-3}, which correlates with the T_1 shortening in Fig. 6(a).

The V_{Si} spin coherence in some other SiC samples [open triangles in Fig. 6(b)] was reported to be longer. It is $T_2 \sim 100$ μs for a single V_{Si} with $N_V \sim 10^{11} - 10^{12}$ cm^{-3} in an epitaxial 4H-SiC layer [27]. Another HPSI 4H-SiC wafer after electron irradiation $\Phi_e = 5 \times 10^{17}$ cm^{-2} gives $T_2 = 81 \pm 4$ μs [7]. As N_V was not reported for this wafer, we assume the same creation yield as in Fig. 2(d) and obtain $N_V \sim 10^{15}$ cm^{-3}. The longer coherence time is likely related to lower concentration of intrinsic paramagnetic centers and hence longer $T_2^{(\text{pristine})}$ compared to that in our nonirradiated wafer [Fig. 6(b)]. The dashed line in Fig. 6(b) represents a fit to Eq. (1) with $T_2^{(\text{pristine})} = 100$ μs and the same κ as in the case above.

Compared to electron irradiation, neutron irradiation creates a higher defect density, but also a higher percentage of defects other than V_{Si}, resulting in a larger κ. As a consequence, the coherence time is significantly shorter for a moderate concentration of the created V_{Si} centers. The coherence time measured for the neutron-irradiated samples should be seen as a lower bound, due to inhomogeneity in the applied microwave field across the detection volume. Application of optimized pulses is required to test the limits of coherence in such samples [58]. Figure 6(b) shows experimental data for HPSI 4H-SiC wafers irradiated in two scientific reactors with different distribution of neutron energy. They can be described assuming $\kappa = 3.8 \times 10^{-11}$ s^{-1} cm^3 and $\kappa = 25.2 \times 10^{-11}$ s^{-1} cm^3 and the same $T_2^{(\text{pristine})} = 48$ μs as for our electron-irradiated wafer, which is represented by the cyan area in Fig. 6(b). We emphasize that for $\Phi_n > 1 \times 10^{17}$ cm^{-2}, when the discrepancy between N_V and N_V^{EPR} becomes significant, the T_2 time is too short and not in favor of quantum applications.

We now compare the aforementioned results to the spin-coherence time in ion-irradiated samples. The ion irradiation can also damage the SiC lattice resulting in a reduction of T_2. It is expected that the irradiation-induced damage is stronger for heavier atoms. From this point of view, it is advantageous to use light atoms—particularly H (protons)—for the creation of highly coherent V_{Si} centers. In the case of low proton irradiation fluence $\Phi_p = 2 \times 10^{11}$ cm^{-2} corresponding to $N_V = 3 \times 10^{13}$ cm^{-3} [Fig. 6(b)], the coherence time $T_2 = 42 \pm 20$ μs approaches that in the pristine wafer $T_2^{(\text{pristine})} = 48$ μs [47]. It was found in another work that with increasing Φ_p and N_V the T_2 time decreases. For $\Phi_p = 1 \times 10^{14}$ cm^{-2} with estimated emitter density $N_V = 3 \times 10^{14}$ cm^{-3}, the spin-coherence time $T_2 = 22 \pm 5$ μs from a stretched exponential fit was reported [50].

In fact, the dependence of the spin coherence on the proton (or any other ion) irradiation fluence is more complex than in the case of electron or neutron irradiation. The ions penetrate to a certain depth, which depends on their energy and the ion type. Though the highest probability to create defects is at the Bragg peak, there is a nonzero probability to create V_{Si} centers between the sample surface and the Bragg peak, which have longer coherence time [11]. We expect that Eq. (1) can still be used for ion irradiation though the parameter κ should depend on the ion type and energy as well as on the depth from the irradiated surface.

B. Effect of annealing

Since, as previously mentioned, a high V_{Si} density combined with long spin coherence is desirable for various applications, we anneal a heavily irradiated sample to explore crystal healing. Figure 7(a) shows the V_{Si} PL spectrum in a neutron-irradiated sample with a fluence $\Phi_n = 1 \times 10^{18}$ cm^{-2} and the corresponding initial emitter density $N_V = 1 \times 10^{16}$ cm^{-3}. Figures 7(c) and 7(d) show the emitter density as a function of the annealing time t_{ann} and temperature T_{ann}, respectively. The PL intensity linked

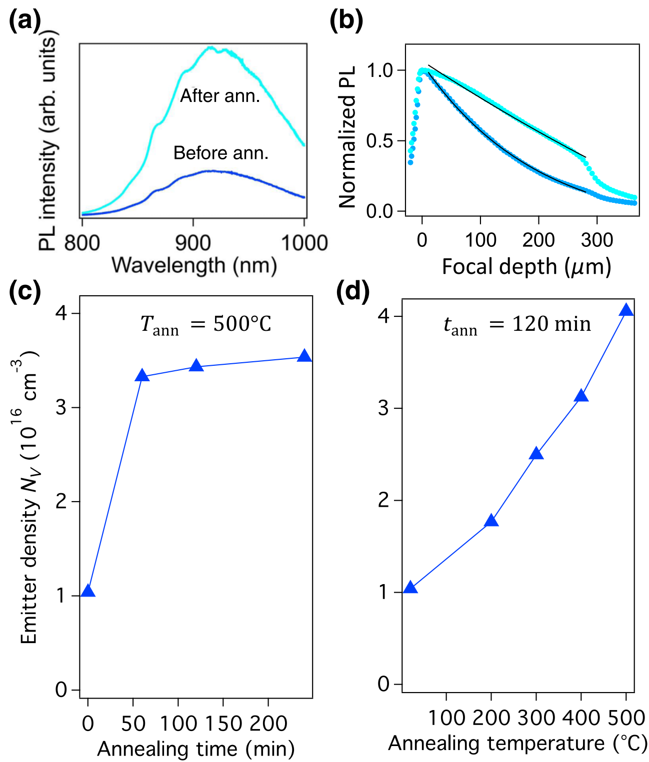

FIG. 7. Effect of annealing on the PL of a heavily neutron-irradiated SiC crystal. The neutron irradiation fluence is $\Phi_n = 1 \times 10^{18}$ cm^{-2}. (a) Increasing of the PL intensity with annealing ($T_{ann} = 500\,^\circ$C and $t_{ann} = 240$ min). (b) PL confocal scans before and after annealing with parameters as in (a). The solid lines are exponential fits. (c) Variation of the emitter density with annealing time at $T_{ann} = 500\,^\circ$C. (d) Variation of the emitter density with annealing temperature for $t_{ann} = 120$ min.

to N_V increases by a factor of 4 after optimum annealing conditions. This increase can be explained by healing of some irradiation-induced and intrinsic defects other than V_{Si}, which can provide nonradiative recombination paths for the V_{Si} defects if they are located in their vicinity. This conclusion is also confirmed by the in-depth (along the z direction) PL scans, presented in Fig. 7(b). Exponential fits to $\exp(-\alpha z)$ allow the estimation of the absorption coefficient $\alpha = \alpha_{laser} + \alpha_{PL}$. It decreases from $\alpha = 50.8$ cm^{-1} to $\alpha = 8.0$ cm^{-1} after annealing, indicating that some color centers are indeed removed.

The annealing temperature in our experiments is limited to $500\,^\circ$C since the V_{Si} defects can otherwise be eliminated at higher temperatures [25]. We note that we neither observe any PL enhancement nor an increase of T_1 or T_2 in the electron-irradiated sample. This again strongly hints at less severe crystal damage and a higher percentage of created V_{Si} centers by electron irradiation.

To explore the effect of annealing on the coherence properties of the V_{Si} defects, we measure T_1 and T_2 in the $\Phi_n = 1 \times 10^{18}$ cm^{-2} sample after each annealing step.

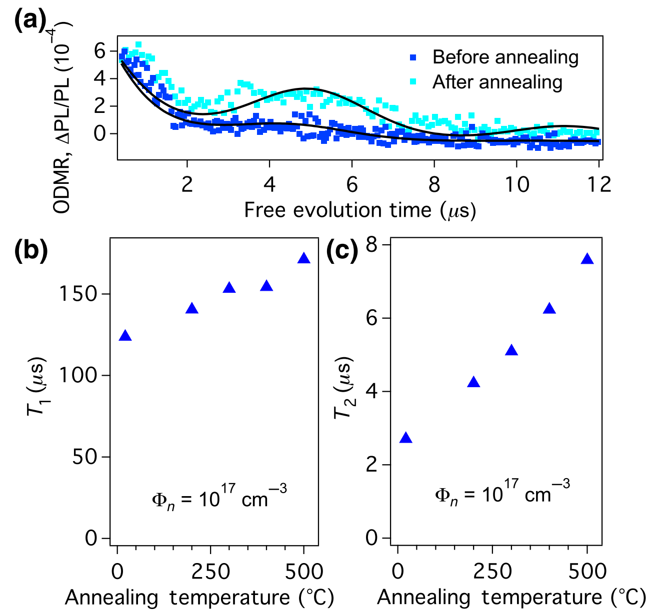

FIG. 8. Effect of annealing on the spin-coherence properties of the V_{Si} defects. (a) ESEEM signal before and after annealing. (b) Evolution of the spin-lattice relaxation time with annealing temperature. (c) Spin-coherence time as a function of annealing temperature. The annealing time for each step in (b),(c) is $t_{ann} = 120$ min.

Figure 8(a) shows the spin-echo experimental data before and after annealing (symbols), fitted with ESEEM (the solid lines). An improvement of the coherence properties with annealing can be clearly seen from these data.

Figure 8(b) presents the measured spin relaxation time T_1 as a function of the annealing temperature ($t_{ann} = 120$ min). Though T_1 increases, it is not completely restored to the value of 300 μs as in the case of low irradiation fluences [Fig. 6(a)]. We note, T_1 as a function of T_{ann} does not saturate in our experiments. For higher T_{ann}, T_1 might increase further, but N_V drops due to healing out of the V_{Si} defects. The spin-coherence time T_2 can be improved by a factor of 2.5 as presented in Fig. 8(c). The maximum value achieved in the heavily irradiated sample is $T_2 = 7.6 \pm 0.5$ μs. Since $1/T_2^{(i)}$ scales with the number of all created defects, this increase of T_2 can be explained by healing of paramagnetic, non-V_{Si} defects at temperatures below 500°C and therefore a suppression of decoherence caused by the spin-spin interaction.

To conclude, we thoroughly investigate the irradiation impact on the room-temperature spin-coherence properties of silicon vacancies in SiC. We measure the spin-lattice relaxation time and the spin-coherence time depending on the irradiation particle (electron, neutron, and proton), irradiation fluence and irradiation energy. In order to find the broader systematics, we analyze the available literature values, too.

We establish that the spin-lattice relaxation time remains constant up to high irradiation fluences, independently of the irradiation type. This is to be expected, as the dominant effect determining the T_1 time is spin-phonon-scattering, which is an intrinsic property of the crystal and therefore, up to a certain level, independent of the fluence. Only for high emitter densities, the interactions between the defects get to play a role for the T_1 time and cause it to drop rapidly.

In contrast, the spin-coherence time is very sensitive to the irradiation type and fluence, indicating a much higher sensitivity regarding the interactions between the defects compared to the T_1 time. The longest spin-coherence time for the same emitter density is observed for electron irradiation. The interaction of electrons with the crystal is mainly limited to ionization. Electrons, which create crystal defects, already lost a lot of energy due to collisions with crystal electrons before. In comparison, neutrons lose almost all of their energy to crystal atoms and thus create much more severe damage than electrons. Surprisingly, the electron energy has no influence on the silicon-vacancy coherence properties and all data can be well described by the same equation with two independent parameters. The shortest spin-coherence time is observed in neutron-irradiated samples, which, however, can be partially recovered using thermal annealing. Since we assume that the dominant effect limiting the T_2 time is $1/T_2^{(i)}$, the increase of the T_2 time in the annealed samples hints at a reduction of the number of irradiation-induced defects other than V_{Si}. This leads to a suppression of the V_{Si} defects' spin decoherence.

We thus expect that our study provides important information for the optimization of the V_{Si} defect spin-coherence properties and allows the design of quantum devices and structures with the desired parameters based on SiC as a platform.

ACKNOWLEDGMENTS

This work is supported by the German Research Foundation (DFG) under Grants No. AS 310/5-1 and No. DY 18/13-1, the FWF project I 3167-N27 SiC-EiC as well as JSPS KAKENHI 17H01056 and 18H03770. V.D. also acknowledges financial support from the DFG through the Würzburg-Dresden Cluster of Excellence on Complexity and Topology in Quantum Matter – ct.qmat (EXC 2147, project-id 39085490). H.K. states that part of this work is carried out at the Jet Propulsion Laboratory, California Institute of Technology, under a contract with the National Aeronautics and Space Administration; and acknowledges funding by the NASA Postdoctoral Program. Z.S. is grateful for support from the China Scholarship Council (CSC File No.: 201706220060). We thank M. Villa and R. Bergmann for operation of the TRIGA reactor as well as G. Bukalis for operation of the BER II reactor.

[1] P. G. Baranov, A. P. Bundakova, A. A. Soltamova, S. B. Orlinskii, I. V. Borovykh, R. Zondervan, R. Verberk, and J. Schmidt, Silicon vacancy in SiC as a promising quantum system for single-defect and single-photon spectroscopy, Phys. Rev. B **83**, 125203 (2011).

[2] W. F. Koehl, B. B. Buckley, F. J. Heremans, G. Calusine, and D. D. Awschalom, Room temperature coherent control of defect spin qubits in silicon carbide, Nature **479**, 84 (2011).

[3] D. Riedel, F. Fuchs, H. Kraus, S. Väth, A. Sperlich, V. Dyakonov, A. Soltamova, P. Baranov, V. Ilyin, and G. V. Astakhov, Resonant Addressing and Manipulation of Silicon Vacancy Qubits in Silicon Carbide, Phys. Rev. Lett. **109**, 226402 (2012).

[4] J. R. Weber, W. F. Koehl, J. B. Varley, A. Janotti, B. B. Buckley, C. G. Van de Walle, and D. D. Awschalom, Quantum computing with defects, Proc. Natl. Acad. Sci. U. S. A. **107**, 8513 (2010).

[5] A. L. Falk, B. B. Buckley, G. Calusine, W. F. Koehl, V. V. Dobrovitski, A. Politi, C. A. Zorman, P. X. L. Feng, and D. D. Awschalom, Polytype control of spin qubits in silicon carbide, Nat. Commun. **4**, 1819 (2013).

[6] L.-P. Yang, C. Burk, M. Widmann, S.-Y. Lee, J. Wrachtrup, and N. Zhao, Electron spin decoherence in silicon carbide nuclear spin bath, Phys. Rev. B **90**, 241203 (2014).

[7] S. G. Carter, Ö. O. Soykal, P. Dev, S. E. Economou, and E. R. Glaser, Spin coherence and echo modulation of the silicon vacancy in 4H-SiC at room temperature, Phys. Rev. B **92**, 161202 (2015).

[8] H. Seo, A. L. Falk, P. V. Klimov, K. C. Miao, G. Galli, and D. D. Awschalom, Quantum decoherence dynamics of divacancy spins in silicon carbide, Nat. Commun. **7**, 12935 (2016).

[9] D. Simin, H. Kraus, A. Sperlich, T. Ohshima, G. V. Astakhov, and V. Dyakonov, Locking of electron spin coherence above 20 ms in natural silicon carbide, Phys. Rev. B **95**, 161201(R) (2017).

[10] M. Fischer, A. Sperlich, H. Kraus, T. Ohshima, G. V. Astakhov, and V. Dyakonov, Highly Efficient Optical Pumping of Spin Defects in Silicon Carbide for Stimulated Microwave Emission, Phys. Rev. Appl. **9**, 2126 (2018).

[11] P. G. Brereton, D. Puent, J. Vanhoy, E. R. Glaser, and S. G. Carter, Spin coherence as a function of implantation depth for silicon vacancies in proton-irradiated 4H-SiC, arXiv:1812.10432

[12] V. A. Soltamov, C. Kasper, A. V. Poshakinskiy, A. N. Anisimov, E. N. Mokhov, A. Sperlich, S. A. Tarasenko, P. G. Baranov, G. V. Astakhov, and V. Dyakonov, Excitation and coherent control of spin qudit modes in silicon carbide at room temperature, Nat. Commun. **10**, 1678 (2019).

[13] H. Kraus, V. A. Soltamov, D. Riedel, S. Väth, F. Fuchs, A. Sperlich, P. G. Baranov, V. Dyakonov, and G. V. Astakhov, Room-temperature quantum microwave emitters based on spin defects in silicon carbide, Nat. Phys. **10**, 157 (2014).

[14] A. L. Falk, P. V. Klimov, B. B. Buckley, V. Ivády, I. A. Abrikosov, G. Calusine, W. F. Koehl, A. Gali, and D. D. Awschalom, Electrically and Mechanically Tunable Electron Spins in Silicon Carbide Color Centers, Phys. Rev. Lett. **112**, 187601 (2014).

[15] Ö. O. Soykal and T. L. Reinecke, Quantum metrology with a single spin-3/2 defect in silicon carbide, Phys. Rev. B **95**, 081405 (2017).

[16] S. Castelletto, B. C. Johnson, and A. Boretti, Quantum effects in silicon carbide hold promise for novel integrated devices and sensors, Adv. Opt. Mater. **1**, 609 (2013).

[17] H. Kraus, V. A. Soltamov, F. Fuchs, D. Simin, A. Sperlich, P. G. Baranov, G. V. Astakhov, and V. Dyakonov, Magnetic field and temperature sensing with atomic-scale spin defects in silicon carbide, Sci. Rep. **4**, 5303 (2014).

[18] D. Simin, F. Fuchs, H. Kraus, A. Sperlich, P. G. Baranov, G. V. Astakhov, and V. Dyakonov, High-Precision Angle-Resolved Magnetometry with Uniaxial Quantum Centers in Silicon Carbide, Phys. Rev. Appl. **4**, 014009 (2015).

[19] S.-Y. Lee, M. Niethammer, and J. Wrachtrup, Vector magnetometry based on S=3/2 electronic spins, Phys. Rev. B **92**, 115201 (2015).

[20] D. Simin, V. A. Soltamov, A. V. Poshakinskiy, A. N. Anisimov, R. A. Babunts, D. O. Tolmachev, E. N. Mokhov, M. Trupke, S. A. Tarasenko, A. Sperlich, P. G. Baranov, V. Dyakonov, and G. V. Astakhov, All-Optical DC Nanotesla Magnetometry Using Silicon Vacancy Fine Structure in Isotopically Purified Silicon Carbide, Phys. Rev. X **6**, 031014 (2016).

[21] M. Niethammer, M. Widmann, S.-Y. Lee, P. Stenberg, O. Kordina, T. Ohshima, N. T. Son, E. Janzén, and J. Wrachtrup, Vector Magnetometry Using Silicon Vacancies in 4H-SiC Under Ambient Conditions, Phys. Rev. Appl. **6**, 034001 (2016).

[22] C. J. Cochrane, J. Blacksberg, M. A. Anders, and P. M. Lenahan, Vectorized magnetometer for space applications using electrical readout of atomic scale defects in silicon carbide, Sci. Rep. **6**, 37077 (2016).

[23] A. N. Anisimov, D. Simin, V. A. Soltamov, S. P. Lebedev, P. G. Baranov, G. V. Astakhov, and V. Dyakonov, Optical thermometry based on level anticrossing in silicon carbide, Sci. Rep. **6**, 33301 (2016).

[24] S. Castelletto, B. C. Johnson, V. Ivády, N. Stavrias, T. Umeda, A. Gali, and T. Ohshima, A silicon carbide room-temperature single-photon source, Nat. Mater. **13**, 151 (2013).

[25] F. Fuchs, B. Stender, M. Trupke, D. Simin, J. Pflaum, V. Dyakonov, and G. V. Astakhov, Engineering near-infrared single-photon emitters with optically active spins in ultrapure silicon carbide, Nat. Commun. **6**, 7578 (2015).

[26] D. J. Christle, A. L. Falk, P. Andrich, P. V. Klimov, J. u. Hassan, N. T. Son, E. Janzén, T. Ohshima, and D. D. Awschalom, Isolated electron spins in silicon carbide with millisecond coherence times, Nat. Mater. **14**, 160 (2015).

[27] M. Widmann, S.-Y. Lee, T. Rendler, N. T. Son, H. Fedder, S. Paik, L.-P. Yang, N. Zhao, S. Yang, I. Booker, A. Denisenko, M. Jamali, S. A. Momenzadeh, I. Gerhardt, T. Ohshima, A. Gali, E. Janzén, and J. Wrachtrup, Coherent control of single spins in silicon carbide at room temperature, Nat. Mater. **14**, 164 (2015).

[28] D. J. Christle, P. V. Klimov, C. F. de las Casas, K. n. Sz sz, V. Iv dy, V. Jokubavicius, J. Ul Hassan, M. Syv j rvi, W. F. Koehl, T. Ohshima, N. T. Son, E. Janz n, d. m. Gali, and D. D. Awschalom, Isolated Spin Qubits in SiC with a High-Fidelity Infrared Spin-to-Photon Interface, Phys. Rev. X **7**, 021046 (2017).

[29] R. Nagy, M. Niethammer, M. Widmann, Y.-C. Chen, P. Udvarhelyi, C. Bonato, J. u. Hassan, R. Karhu, I. G. Ivanov, N. T. Son, J. R. Maze, T. Ohshima, Ö. O. Soykal, A. Gali, S.-Y. Lee, F. Kaiser, and J. Wrachtrup, High-fidelity spin and optical control of single silicon-vacancy centres in silicon carbide, Nat. Commun. **10**, 1954 (2019).

[30] H. B. Banks, Ö. O. Soykal, R. L. Myers-Ward, D. K. Gaskill, T. L. Reinecke, and S. G. Carter, Resonant Optical Spin Initialization and Readout of Single Silicon Vacancies in 4H-SiC, Phys. Rev. Appl. **11**, 024013 (2019).

[31] S. J. Whiteley, G. Wolfowicz, C. P. Anderson, A. Bourassa, H. Ma, M. Ye, G. Koolstra, K. J. Satzinger, M. V. Holt, F. J. Heremans, A. N. Cleland, D. I. Schuster, G. Galli, and D. D. Awschalom, Spin–phonon interactions in silicon carbide addressed by Gaussian acoustics, Nat. Phys. **15**, 490 (2019).

[32] A. V. Poshakinskiy and G. V. Astakhov, Optically detected spin-mechanical resonance in silicon carbide membranes, Phys. Rev. B **100**, 094104 (2019).

[33] G. Calusine, A. Politi, and D. D. Awschalom, Silicon carbide photonic crystal cavities with integrated color centers, Appl. Phys. Lett. **105**, 011123 (2014).

[34] D. O. Bracher and E. L. Hu, Fabrication of high-Q nanobeam photonic crystals in epitaxially grown 4H-SiC, Nano. Lett. **15**, 6202 (2015).

[35] M. Radulaski, M. Widmann, M. Niethammer, J. L. Zhang, S.-Y. Lee, T. Rendler, K. G. Lagoudakis, N. T. Son, E. Janzén, T. Ohshima, J. Wrachtrup, and J. Vučković, Scalable quantum photonics with single color centers in silicon carbide, Nano. Lett. **17**, 1782 (2017).

[36] A. Lohrmann, T. J. Karle, V. K. Sewani, A. Laucht, M. Bosi, M. Negri, S. Castelletto, S. Prawer, J. C. McCallum, and B. C. Johnson, Integration of single-photon emitters into 3C-SiC microdisk resonators, ACS Photonics **4**, 462 (2017).

[37] F. Fuchs, V. A. Soltamov, S. Väth, P. G. Baranov, E. N. Mokhov, G. V. Astakhov, and V. Dyakonov, Silicon carbide light-emitting diode as a prospective room temperature source for single photons, Sci. Rep. **3**, 1637 (2013).

[38] A. Lohrmann, N. Iwamoto, Z. Bodrog, S. Castelletto, T. Ohshima, T. J. Karle, A. Gali, S. Prawer, J. C. McCallum, and B. C. Johnson, Single-photon emitting diode in silicon carbide, Nat. Commun. **6**, 7783 (2015).

[39] M. Niethammer, M. Widmann, T. Rendler, N. Morioka, Y.-C. Chen, R. Stöhr, J. U. Hassan, S. Onoda, T. Ohshima, S.-Y. Lee, A. Mukherjee, J. Isoya, N. T. Son, and J. Wrachtrup, Coherent electrical readout of defect spins in 4H-SiC by photo-ionization at ambient conditions, Nat. Commun. **10**, 5569 (2019).

[40] S. Castelletto, B. C. Johnson, C. Zachreson, D. Beke, I. Balogh, T. Ohshima, I. Aharonovich, and A. Gali, Room temperature quantum emission from cubic silicon carbide nanoparticles, ACS Nano **8**, 7938 (2014).

[41] A. Muzha, F. Fuchs, N. V. Tarakina, D. Simin, M. Trupke, V. A. Soltamov, E. N. Mokhov, P. G. Baranov, V. Dyakonov, A. Krueger, and G. V. Astakhov, Room-temperature near-infrared silicon carbide nanocrystalline

emitters based on optically aligned spin defects, Appl. Phys. Lett. **105**, 243112 (2014).

[42] Y.-C. Chen, P. S. Salter, M. Niethammer, M. Widmann, F. Kaiser, R. Nagy, N. Morioka, C. Babin, J. Ü. Erlekampf, P. Berwian, M. Booth, and J. Wrachtrup, Laser wrtiing of scalable single colour centre in silicon carbide, Nano. Lett. **19**, 2377 (2019).

[43] E. Sörman, N. Son, W. Chen, O. Kordina, C. Hallin, and E. Janzén, Silicon vacancy related defect in 4H and 6H SiC, Phys. Rev. B **61**, 2613 (2000).

[44] H. J. von Bardeleben, J. L. Cantin, L. Henry, and M. F. Barthe, Vacancy defects in p-type 6H-SiC created by low-energy electron irradiation, Phys. Rev. B **62**, 10841 (2000).

[45] H. L. Heinisch, L. R. Greenwood, W. J. Weber, and R. E. Williford, Displacement damage in silicon carbide irradiated in fission reactors, J. Nucl. Mater. **327**, 175 (2004).

[46] H. von Bardeleben, J. Cantin, I. Vickridge, and G. Battistig, Proton-implantation-induced defects in n-type 6H- and 4H-SiC: An electron paramagnetic resonance study, Phys. Rev. B **62**, 10126 (2000).

[47] H. Kraus, D. Simin, C. Kasper, Y. Suda, S. Kawabata, W. Kada, T. Honda, Y. Hijikata, T. Ohshima, V. Dyakonov, and G. V. Astakhov, Three-dimensional proton beam writing of optically active coherent vacancy spins in silicon carbide, Nano. Lett. **17**, 2865 (2017).

[48] J. Wang, X. Zhang, Y. Zhou, K. Li, Z. Wang, P. Peddibhotla, F. Liu, S. Bauerdick, A. Rudzinski, Z. Liu, and W. Gao, Scalable fabrication of single silicon vacancy defect arrays in silicon carbide using focused ion beam, ACS Photonics **4**, 1054 (2017).

[49] J. Wang, Y. Zhou, X. Zhang, F. Liu, Y. Li, K. Li, Z. Liu, G. Wang, and W. Gao, Efficient Generation of an Array of Single Silicon-Vacancy Defects in Silicon Carbide, Phys. Rev. Appl. **7**, 064021 (2017).

[50] J. S. Embley, J. S. Colton, K. G. Miller, M. A. Morris, M. Meehan, S. L. Crossen, B. D. Weaver, E. R. Glaser, and S. G. Carter, Electron spin coherence of silicon vacancies in proton-irradiated 4H-SiC, Phys. Rev. B **95**, 045206 (2017).

[51] J.-F. Wang, Q. Li, F.-F. Yan, H. Liu, G.-P. Guo, W.-P. Zhang, X. Zhou, L.-P. Guo, Z.-H. Lin, J.-M. Cui, X.-Y. Xu, J.-S. Xu, C.-F. Li, and G.-C. Guo, On-demand generation of single silicon vacancy defects in silicon carbide, ACS Photonics **6**, 1736 (2019).

[52] B. Campbell and A. Mainwood, Radiation damage of diamond by electron and gamma irradiation, Phys. Status Solidi A **181**, 99 (2000).

[53] P. Sigmund, *Particle Penetration and Radiation Effects*, Springer Series in Solid-State Sciences Vol. 151 (Springer Berlin Heidelberg, Berlin, Heidelberg, 2006).

[54] E. Wendler, T. Bierschenk, F. Felgenträger, J. Sommerfeld, W. Wesch, D. Alber, G. Bukalis, L. C. Prinsloo, N. van der Berg, E. Friedland, and J. B. Malherbe, Damage formation and optical absorption in neutron irradiated SiC, Nucl. Instrum. Methods Phys. Res. B **286**, 97 (2012).

[55] T. C. Hain, F. Fuchs, V. A. Soltamov, P. G. Baranov, G. V. Astakhov, T. Hertel, and V. Dyakonov, Excitation and recombination dynamics of vacancy-related spin centers in silicon carbide, J. Appl. Phys. **115**, 133508 (2014).

[56] P. L. Stanwix, L. M. Pham, J. R. Maze, D. Le Sage, T. K. Yeung, P. Cappellaro, P. R. Hemmer, A. Yacoby, M. D. Lukin, and R. L. Walsworth, Coherence of nitrogen-vacancy electronic spin ensembles in diamond, Phys. Rev. B **82**, 201201 (2010).

[57] E. Bauch, C. A. Hart, J. M. Schloss, M. J. Turner, J. F. Barry, P. Kehayias, S. Singh, and R. L. Walsworth, Ultralong Dephasing Times in Solid-State Spin Ensembles via Quantum Control, Phys. Rev. X **8**, 031025 (2018).

[58] T. Nöbauer, A. Angerer, B. Bartels, M. Trupke, S. Rotter, J. Schmiedmayer, F. Mintert, and J. Majer, Smooth Optimal Quantum Control for Robust Solid-State Spin Magnetometry, Phys. Rev. Lett. **115**, 190801 (2015).